Article

Polypyrrole/Carbon Nanotube Freestanding Electrode with Excellent Electrochemical Properties for High-Performance All-Solid-State Supercapacitors

Jincy Parayangattil Jyothibasu, Ming-Zhu Chen, and Rong-Ho Lee*

Read Online

ACCESS | Metrics & More | Article Recommendations | SI Supporting Information

ABSTRACT: In this study, a facile and environmentally friendly method was used to prepare a freestanding supercapacitor electrode displaying excellent areal capacitance and good cycle life performance. First, we prepared polypyrrole nanoparticles (PPyNP) through a simple *in situ* chemical polymerization using the plant-derived material curcumin as a bioavailable template. A PPyNP/f-CNT freestanding composite electrode of high mass loading (ca. 14 mg cm^{-2}) was prepared after blending the mixtures of the prepared PPyNP and functionalized CNTs (f-CNTs). The performance of the as-prepared material as a supercapacitor electrode was evaluated in a three-electrode setup using aqueous 1 M H$_2$SO$_4$ as the electrolyte. The PPyNP/f-CNT freestanding composite electrode exhibited a high areal capacitance of 4585 mF cm^{-2} and a corresponding volumetric capacitance of 176.35 F cm^{-3} at a current density of 2 mA cm^{-2}. A symmetric all-solid-state supercapacitor assembled using two identical pieces of PPyNP/f-CNT composite electrodes exhibited maximum areal energy and power density of 129.24 μW h cm^{-2} and 12.5 mW cm^{-2}, respectively. Besides, this supercapacitor device exhibited good cycle life performance, with 79.03% capacitance retention after 10,000 charge/discharge cycles. These results suggest practical applications for these PPyNP/f-CNT freestanding composite electrode-based symmetric all-solid-state supercapacitors.
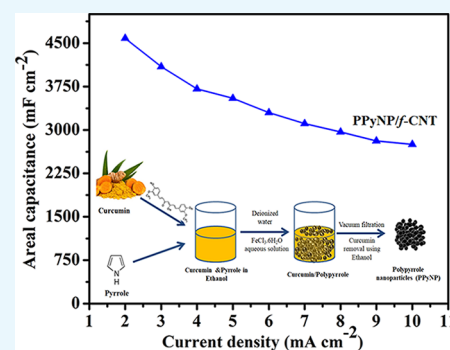
1. INTRODUCTION

The ever-growing market for wearable electro-optical devices has intensified the need for inexpensive, reliable, lightweight, eco-friendly, and safe energy storage devices.[1,2] Electrochemical supercapacitors have several attractive features, including large power density, fast charging/discharging rates, high cycling stability, low fabrication costs, and environmental friendliness, which make them promising energy sources for such electronic devices.[3,4] Nevertheless, the low energy densities of conventional supercapacitors have limited their practical applications.[5] To enhance the energy densities, it will be necessary to design electrode materials to have high capacitances, large electrochemically accessible surface areas, suitable porous structures, and high electrical conductivities.[6] During the fabrication of conventional supercapacitor electrodes, the active materials are usually mixed with binders and conductive additives, with the resulting slurries pressed onto metallic current collectors. Adding these inactive components enhances the cost of electrode fabrication and the total weight of the devices, making them less compatible with portable and wearable electronics. Moreover, the inherent resistance of the binder materials decreases the electrode's surface area and conductivity, leading to a low electrochemical reaction rate, further hindering the applicability in high-performance supercapacitors.[7] Thus, to achieve high performance, it will be necessary to fabricate freestanding supercapacitor electrodes

that do not involve binders, conductive additives, or current collectors.

Polypyrrole (PPy) is a promising candidate for supercapacitor electrodes because of its large theoretical capacitance, good redox properties, superior conductivity, ease of synthesis, nontoxicity, biocompatibility, and high thermal and environmental stability.[8−10] Unfortunately, pristine PPy usually undergoes structural damage when subjected to long-term cycling because of the repeated swell−shrink behavior of the polymer backbone during the ion doping and dedoping processes of PPy, resulting in more unsatisfactory electrochemical performance and lower cyclic stability when compared with carbon-based materials.[11−14] Significant improvements in the electrochemical energy storage ability and cycling charge−discharge stability of PPy-based electrodes can be realized by properly tuning the size and morphology of the PPy to enhance the specific surface area and porosity.[15] Compared with their bulk counterparts, nanostructured forms of PPy (*e.g.*, nanospheres,[4,16,17] nanosheets,[18] nanorods/tubes/
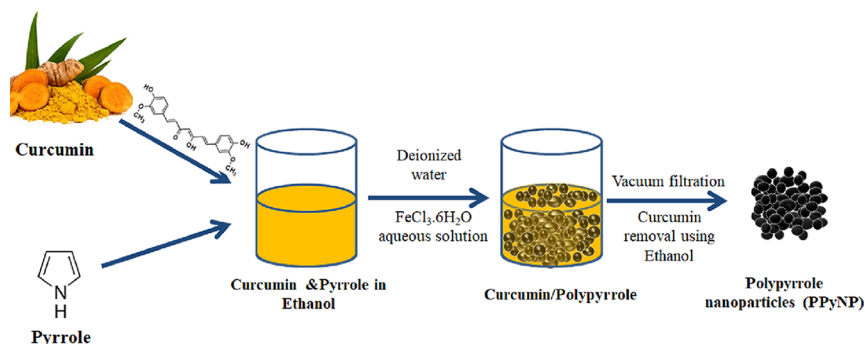
Figure 1. Schematic representation of the preparation of PPy nanoparticles (PPyNP).

wires,[10,19−22] and nanobrushes[23]) can have significantly greater effective surface areas and porosities that, in turn, result in greater use of active materials by shortening the diffusion path for ions to maximize electrolyte exposure.[4,7] The morphologies and thereby the subsequent electrochemical property of the PPy nanostructures are highly related to the synthetic methods used for their preparation. Such nanoscale PPy structures are commonly prepared using chemical oxidative polymerization,[5,17,24,25] vapor phase polymerization,[23,26] electropolymerization,[27] and interfacial polymerization[15,22,28,29] in the presence of hard or soft templates to fine-tune the final morphologies. The syntheses involving the hard templates require harsh post-treatment processes to etch away the hard templates and recover the pristine PPy nanostructures, making such processes complex and time-consuming.[4] Therefore, soft-template methods, involving surfactant micelles, functionalized organic acids, or polymeric stabilizers, are preferred over hard-template methods for the formation of desired morphologies of PPy. Although the syntheses of PPy nanostructures using various soft templates (*e.g.*, cetyltrimethylammonium bromide,[22] sodium dodecylbenzene sulfonate,[5,24] and *N*-methylene phosphonic chitosan[17]) can be simple and effective, they can be expensive and possibly environmentally contaminating when prepared on bulk scales. Therefore, for the bulk production of PPy nanostructures, the quest remains to develop synthetic methods that are less complicated, more environmentally friendly, less time-consuming, less expensive, cleaner, and more efficient.

To improve its electrochemical properties and cycling stability, PPy is often combined with carbon-based electrical double-layer capacitance (EDLC) materials to form nanocomposite electrodes. Carbon nanotubes (CNTs) are particularly effective additives for forming highly efficient supercapacitor electrodes with PPy because of their exceptional mechanical properties, large surface areas, and superior electrical conductivities. Composite electrodes developed from combinations of PPy and CNTs have displayed enhanced electrochemical properties in terms of improved cycling stabilities, power densities, and rate capabilities. In addition, CNTs can also increase the mechanical strength of PPy/CNT-based composites by serving as structural-reinforcing agents. Taking advantage of the synergy between CNTs with high conductivity and PPy with high energy density, PPy/CNT nanocomposites can effectively mitigate the drawbacks of the low specific capacitance of CNTs and the poor cycling life of PPy. Nevertheless, the synthetic routes for the preparation of PPy/CNT nanocomposites can have a great influence on their structural and electrochemical properties. For example, most previously reported PPy/CNT nanocomposites have been

synthesized through *in situ* chemical polymerization of the pyrrole in a dispersion containing CNT; they have been obtained in powder form and thereby have required the use of binders, conductive additives, and current collectors to fabricate supercapacitor electrodes.[30−32] Accordingly, efforts have been made to fabricate freestanding PPy/CNT nanocomposites involving the direct growth of PPy through chemical polymerization or electrodeposition on preformed CNT films, thereby enabling high interfacial conductance between PPy and CNT and resulting in improved supercapacitor performance. It has been difficult, however, to deposit large amounts of PPy on CNTs without blocking the electrolyte channels when using such methods.[33,34] This limited mass loading results in poor areal capacitance—an undesirable feature for practical applications.[35] In general, electrodes with very low active-material mass loadings often result in overestimated gravimetric capacitance values.[36] In reality, the gravimetric capacitance will not increase upon increasing the active-material loading; instead, performance matrices of the supercapacitor will all tend to decrease accordingly. Therefore, to achieve a true estimation of the electrochemical properties of the supercapacitors for practical applications, the supercapacitor electrodes must be prepared with high mass loadings of the active materials (>10 mg cm^{-2}).[37] Nevertheless, achieving a high energy/power density, rate performance, and cycling charge−discharge stability at a high mass loading remains a scientific challenge.[38]

In this study, a composite film based on PPy nanoparticles and *f*-CNTs was fabricated through a green route using the plant-derived material curcumin as a template. The as-prepared composite film was then directly used as a freestanding electrode for supercapacitors. The electrode with high mass loading achieved a superior areal capacitance of 4585 mF cm^{-2} and an excellent volumetric capacitance of 176.35 F cm^{-3}. Furthermore, the symmetric supercapacitor cell assembled using the binder-free electrodes exhibited maximum areal energy and power density of 129.24 μW h cm^{-2} and 12.5 mW cm^{-2}, respectively, and excellent cycle life (retained 79.03% capacitance after 10,000 cycles).

2. RESULTS AND DISCUSSION

The fabrication process of the PPyNP/*f*-CNT nanocomposite film is illustrated in Figure 1. First, curcumin and the pyrrole monomer were dissolved in ethanol. Curcumin is a natural polyphenol produced by the plant *Curcuma longa* of the ginger family.[39] Curcumin is poorly soluble in water because of its aromatic rings. Therefore, the addition of water resulted in the precipitation of curcumin crystals, which could serve as

anchoring sites for the pyrrole monomer due to the hydrophobic nature of its phenyl rings and the potential for hydrogen bonding of its side groups with the NH unit of pyrrole.[40,41] The addition of aqueous ferric chloride solution initiated the polymerization of pyrrole. After the polymerization was complete, anhydrous ethanol was used to remove the curcumin template and obtain the interconnected PPy nanoparticles.

SEM and TEM were used to study the nanostructure of the PPy samples prepared with and without curcumin. The presence of curcumin in the polymerization medium had a strong influence on the morphology and size of the PPy nanoparticles. In the absence of the curcumin template, PPyC was formed as dense irregular agglomerates with sizes ranging from 200 to 300 nm (Figure 2a). These agglomerated
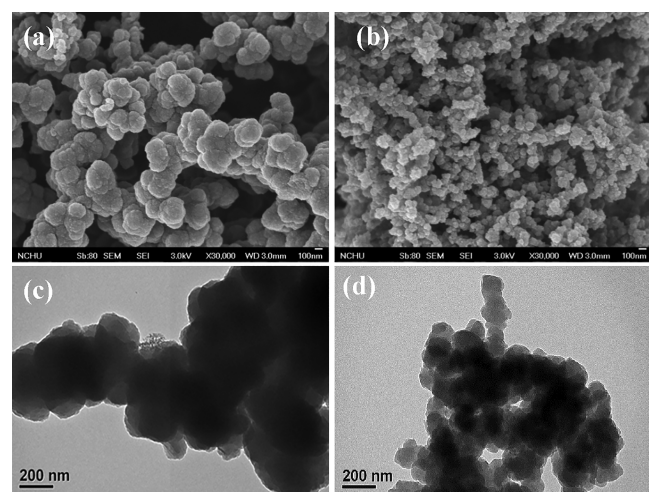
Figure 2. (a,b) SEM and (c,d) TEM images of (a,c) PPyC and (b,d) PPyNP.

structures hinder the movement of electrolyte ions. When the polymerization was performed in the presence of the curcumin template, the PPyNP structures were considerably smaller (60−80 nm) and the interconnected nanoparticles formed a loosely porous morphology (Figure 2b). The porous morphology of PPyNP would enhance the interfacial area between the PPy nanoparticles and the electrolyte, promoting maximum active-material utilization. Moreover, a ready infiltration of electrolytes into the porous composite film matrix would facilitate the rapid movement of ions during charge/discharge processes. The TEM images of PPyC and
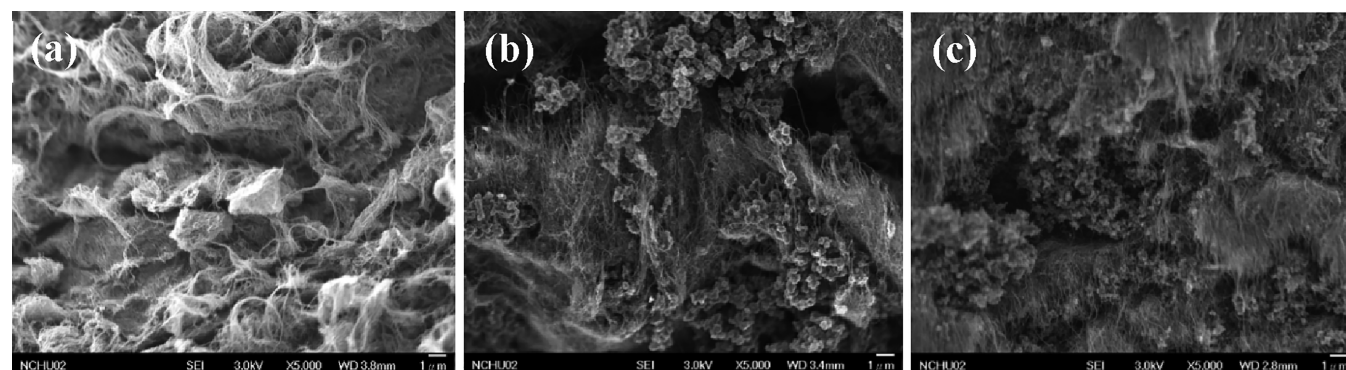
PPyNP were in agreement with the SEM images. PPyNP in Figure 2d reveals interconnected PPy nanoparticles forming a porous structure; in contrast, a dense agglomerated morphology was observed in the TEM image of PPyC (Figure 2c).

Figure 3 presents the SEM images of freestanding films of *f*-CNT, PPyC/*f*-CNT, and PPyNP/*f*-CNT, respectively. The image in Figure 3a reveals a porous conductive network of entangled *f*-CNTs. For both the PPyC/*f*-CNT and PPyNP/*f*-CNT freestanding electrodes, the *f*-CNTs provided structural integrity and enabled the formation of highly conductive freestanding films without the need for any polymer binder, conductive additives, or current collector. In the absence of the *f*-CNTs, it was not possible to form freestanding electrodes because of the poor mechanical integrity of the pristine PPyC and PPyNP.

FTIR spectra of the PPyC, PPyNP, *f*-CNT, and PPyNP/*f*-CNT composite films are shown in Figure 4. Figure S1
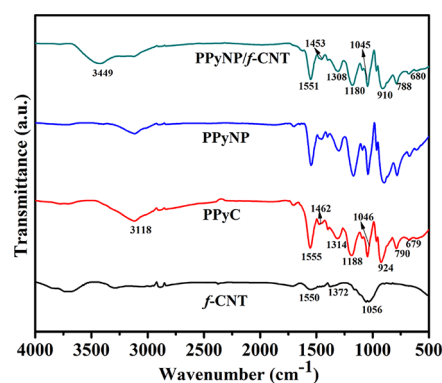

Figure 4. FTIR spectra of *f*-CNT, PPyC, PPyNP, and the PPyNP/*f*-CNT freestanding composite film.

presents the FTIR spectrum of curcumin. The absorption bands at 3510 and 2849 cm^{-1} may be designated as the O−H vibration and C−H stretching vibration of the OCH$_3$ unit, respectively.[42] The absorption peak at 1628 cm^{-1} is due to the stretching vibrations of the C=O and C=C units.[43] The other characteristic absorption peaks at 1510, 1430, 1376, and 1283 cm^{-1} represent the stretching vibrations of the C=O group,[43] olefinic C−H bending vibration,[42] the CH$_3$ bending vibration,[42] and the aromatic enol C−O stretching,[43] respectively. The absorption peaks of the symmetric and asymmetric C−O−C vibrations appear at 1154 and 1027 cm^{-1}.[43] The absorption peaks at 964, 814, and 714 cm^{-1}

Figure 3. SEM images of (a) *f*-CNT, (b) PPyC/*f*-CNT, and (c) PPyNP/*f*-CNT composite films.

represent the benzoate *trans*-CH vibration,[43] the out-of-plane C−CH vibrations of the aromatic rings,[42] and *cis*-CH vibrations of the aromatic rings, respectively.[43] The absorption peaks of curcumin were absent from the FTIR spectrum of PPyNP, but it displayed the characteristic signals of pure PPy, similar to those in the spectrum of PPyC. In the spectra of PPyC and PPyNP, a broad band centered around 3118 cm⁻¹ is designated as the N−H stretching vibration of the pyrrole ring.[10,44] The small absorption band at 2890 cm⁻¹ may be assigned to the symmetric vibrations of the CH₂ units.[45] The band at 1555 cm⁻¹ is due to the combination of C═C and C−C stretching vibrations of PPy.[46] The signal appearing at 1462 cm⁻¹ is ascribed to C−N stretching vibrations, while the band at 1314 cm⁻¹ represents the C−H and C−N in-plane deformation modes.[47] The absorption bands near 1188 and 924 cm⁻¹ indicate the presence of a doped PPy state.[46,48] The absorption band at 1046 cm⁻¹ is designated as the C−H in-plane deformation vibration of the PPy ring,[46] while the signal at 790 cm⁻¹ is due to the C−H out-of-plane ring deformations.[47] The characteristic absorption bands of PPy underwent various redshifts in the FTIR spectrum of the PPyNP/*f*-CNT nanocomposite, suggesting strong interactions between PPyNP and *f*-CNT in this composite.[49] The broad band near 3449 cm⁻¹ represents the O−H stretching vibration in *f*-CNT.

Figure 5 displays the XRD patterns of the prepared samples. For *f*-CNTs, one broad peak assigned to the (002) lattices of
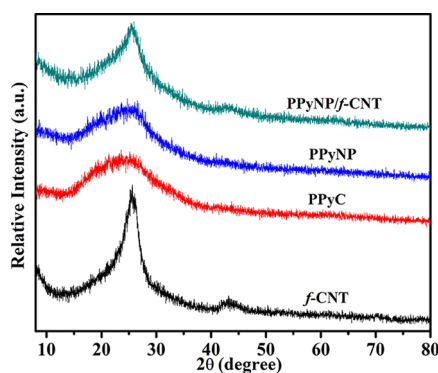

Figure 5. XRD patterns of the *f*-CNTs, PPyC, PPyNP, and the PPyNP/*f*-CNT freestanding composite film.

hexagonal graphite has appeared at 2θ = 25.6°; a low-intensity peak appeared at 43.4°, corresponding to diffractions of the graphitic planes (110) and (100) collectively. In the XRD patterns of PPyC and PPyNP, the characteristic broad diffraction peak of PPy was centered at about 2θ = 25°, revealing an amorphous nature of the PPy.[4,45] The characteristic high-intensity diffraction peaks of curcumin were located at values of 2θ of 8.9, 12.2, 14.5, 15.7, 17.3, 19.5, 21.3, 23.8, 26.1, 28.9, and 31.6° in the XRD pattern, indicating its well-developed crystalline nature.[43,50] The diffraction peaks of PPyNP were almost identical to those of PPyC, indicating the formation of pristine PPy nanoparticles without the introduction of additional peaks resulting from the presence of curcumin. In the XRD pattern of the PPyNP/*f*-CNT nanocomposite, the broad peak of the PPy polymer backbone merged with the *f*-CNT peak at 2θ = 25°. In addition, the low-intensity peak of the *f*-CNTs near 43° also appeared in the XRD pattern of the PPyNP/*f*-CNT nanocomposite.

An electrode material having a large effective surface area increases the electrolyte accessibility and thereby allows complete utilization of the active materials during the electrochemical processes. Thus, their surface area and pore distribution in the electrode both play critical roles in determining the electrochemical properties. Figure 6 and Figure S2 demonstrate the N₂ sorption isotherms of the samples. The composite films provided type-IV isotherms, indicative of porous structures that were mainly composed of mesopores. The BET surface area of the *f*-CNTs was 270.6 m² g⁻¹, and the average pore diameter was 21.42 nm. The specific surface area of PPyNP (32.5 m² g⁻¹) was much larger compared with that of PPyC (12.4 m² g⁻¹). PPyNP and PPyC displayed average pore diameters of 18.2 and 23.0 nm, respectively, confirming their mesoporous structures. We attribute the low specific surface area of PPyC to the agglomeration of the PPy nanoparticles resulting in a compact morphology, which was clearly observed in the TEM and SEM images. The specific surface areas of the PPyNP/*f*-CNT and the PPyC/*f*-CNT composites were 85.6 m² g⁻¹ and 31.03 m² g⁻¹, respectively. The high specific surface areas of the PPyNP/*f*-CNT and PPyC/*f*-CNT composites, compared with those of pure PPyNP and PPyC, might result from the incorporation of the *f*-CNTs with a larger surface area. Apart from that, the average pore diameters of the PPyNP/*f*-CNT and the PPyC/*f*-CNT composites, calculated from the BJH pore size distribution curves, were 17.24 and 30.49 nm, respectively, confirming that the porous structure was dominated by mesopores. The PPyNP/*f*-CNT freestanding composite with a higher specific surface area, coupled with suitable pore distributions, would provide a high electrolyte contact area that might potentially facilitate rapid ion diffusion.

The wettability of *f*-CNTs, PPyC/*f*-CNT, and PPyNP/*f*-CNT freestanding films was measured using water contact angle analysis (Figure 7). The wetting behavior of a porous film is governed mainly by the chemical composition, the geometrical structure of solid surfaces, and the capillary forces induced by strong intermolecular interactions between the liquid and the substance.[51,52] The water contact angle of PPyNP/*f*-CNT film (39.35°) is slightly smaller than that of *f*-CNT (44.58°) and PPyC/*f*-CNT (44.62°) films, indicating its good wettability. The better wetting behavior of the PPyNP/*f*-CNT composite film would suggest ready penetration of the electrolyte into the porous freestanding electrode matrix, potentially enabling maximum use of the active materials.

The electrochemical behaviors of the *f*-CNT-, PPyC/*f*-CNT-, and PPyNP/*f*-CNT-based composites were evaluated in a three-electrode setup. Figure 8a presents the CV (cyclic voltammetry) plots measured at a 5 mV s⁻¹ scan rate. The *f*-CNT electrode displayed a CV curve that is close to a rectangular shape, indicative of an almost ideal electrical double-layer capacitance. PPyNP/*f*-CNT and PPyC/*f*-CNT electrodes exhibited quasi-rectangular curves, indicative of the capacitance being contributed by the PPy (pseudocapacitance) and the *f*-CNTs (double-layer capacitance). The PPyNP/*f*-CNT-based electrode displayed a much larger integrated area inside the CV curve than *f*-CNT- and PPyC/*f*-CNT-based electrodes, revealing the former's superior capacitance. Figure 8b provides the GCD (galvanostatic charge/discharge) curves recorded at a 2 mA cm⁻² current density. The *f*-CNT-based electrode with a highly symmetric triangular-shaped charge/discharge curve confirmed its typical double-layer capacitance behavior with good electrochemical reversibility. The existence
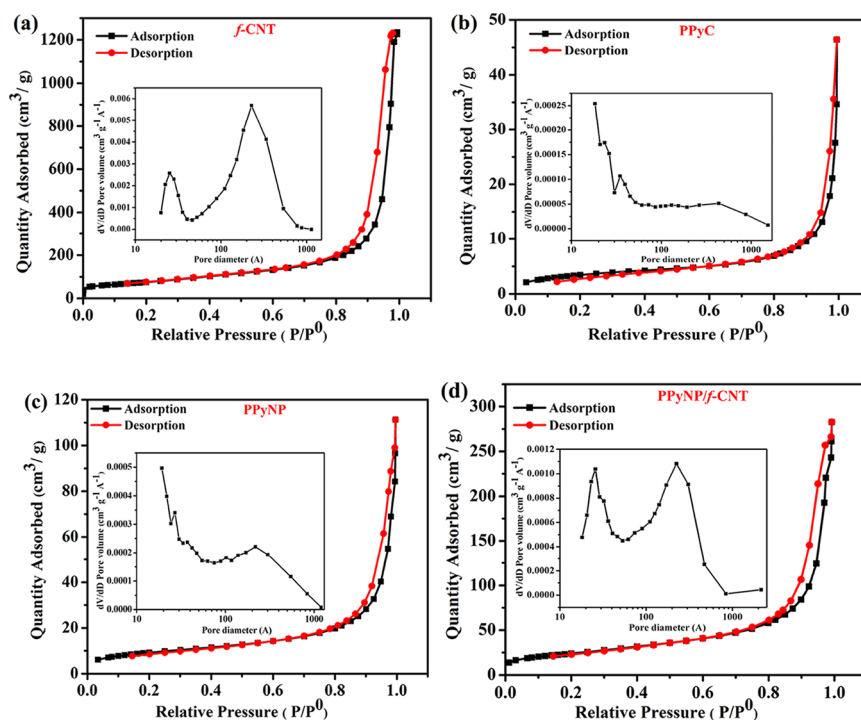
Figure 6. Nitrogen sorption isotherms of (a) *f*-CNTs, (b) PPyC, (c) PPyNP, and (d) PPyNP/*f*-CNT freestanding film. Inset: pore size distribution curves.
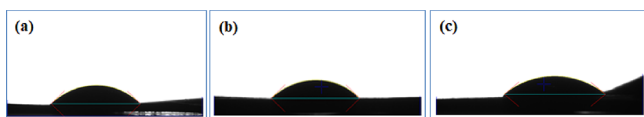

Figure 7. Contact angle measurements. Photographs of water droplets on (a) *f*-CNT, (b) PPyC/*f*-CNT, and (c) PPyNP/*f*-CNT freestanding films.

of pseudocapacitive behavior in both the PPyNP/*f*-CNT- and PPyC/*f*-CNT-based composites was confirmed by their slightly distorted triangular-shaped GCD curves. The PPyNP/*f*-CNT electrode had the longest discharge time and the highest areal capacitance (4585 mF cm^{-2}) compared with the *f*-CNT electrode (563 mF cm^{-2}) and the PPyC/*f*-CNT based electrode (3611 mF cm^{-2}). Besides, the PPyNP/*f*-CNT-based electrode attained corresponding gravimetric and volumetric capacitances of 327.5 F g^{-1} and 176.35 F cm^{-3}, respectively. The areal, gravimetric, and volumetric capacitan-

ces obtained for the PPyNP/*f*-CNT-based electrode were larger than those reported previously for PPy-based composite electrodes (Table S1). We attribute the higher capacitance of the PPyNP/*f*-CNT electrode to the greater use of the inner active redox sites in its PPyNP structure, resulting from the larger active surface area and greater wettability of this composite electrode and its porous architecture that facilitated rapid electrolyte ion diffusion. The electrolyte ions could not access the interior of the PPyC in the case of the PPyC/*f*-CNT freestanding electrode due to its more compact structure that hindered the electrolyte diffusion, leading to an inferior capacitance.

Figure 9 displays the CV plots of the PPyC/*f*-CNT-, PPyNP/*f*-CNT-, and *f*-CNT-based electrodes measured at different scan rates. As revealed in Figure 9a−c, at all of the tested scan rates, the current responses of the PPyNP/*f*-CNT-based electrode were much larger compared with the *f*-CNT- and PPyC/*f*-CNT-based electrodes, indicating its superior
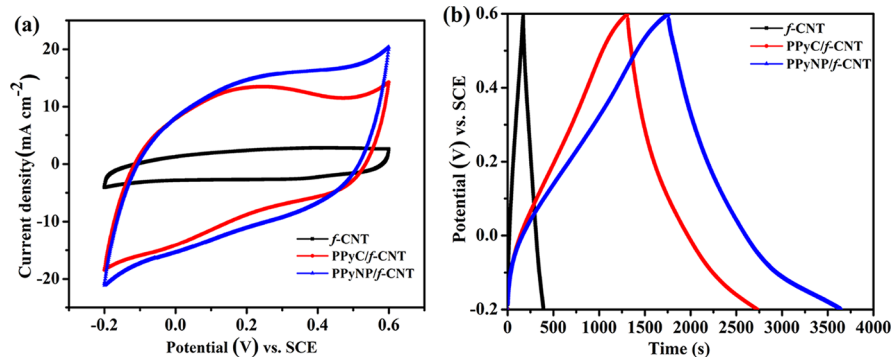
Figure 8. Electrochemical behavior of the *f*-CNT, PPyC/*f*-CNT, and PPyNP/*f*-CNT electrodes: (a) CV curves and (b) GCD curves measured at a 5 mV s^{-1} scan rate and a 2 mA cm^{-2} current density, respectively.
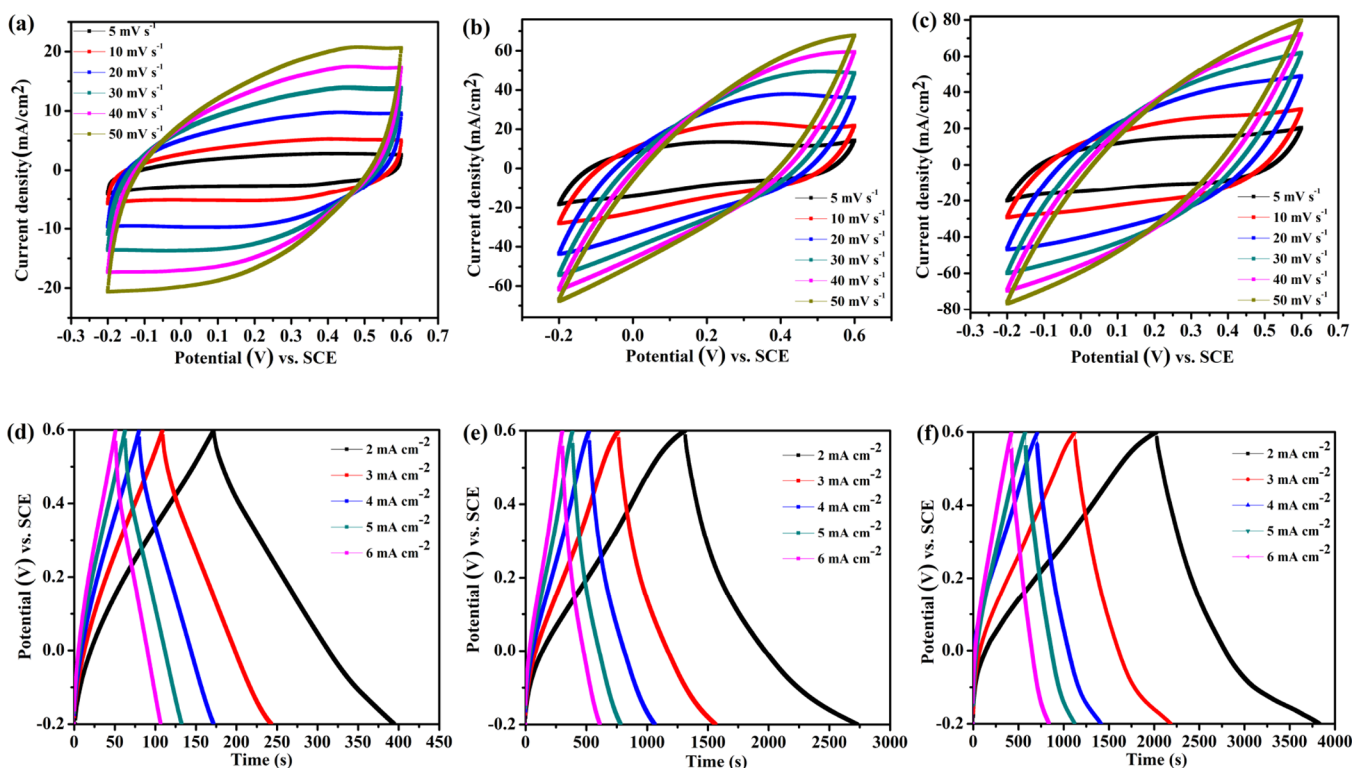
Figure 9. (a−c) CV and (d−f) GCD plots at various current densities of (a,d) *f*-CNT, (b,e) PPyC/*f*-CNT, and (c,f) PPyNP/*f*-CNT electrodes.
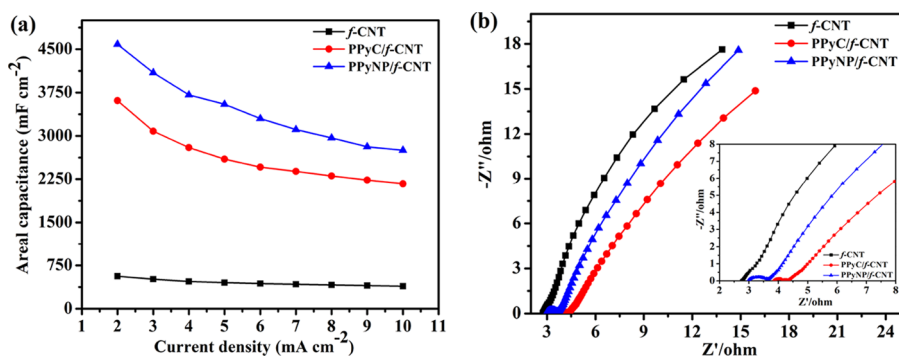
Figure 10. (a) Areal capacitances vs. current density plot and (b) EIS spectra of the *f*-CNT-, PPyC/*f*-CNT-, and PPyNP/*f*-CNT-based electrodes.

capacitance properties. The GCD plots of the *f*-CNT-, PPyC/*f*-CNT-, and PPyNP/*f*-CNT-based electrodes (Figure 9d−f, respectively) revealed that the *f*-CNT-based electrode provided symmetric triangular-shaped charge−discharge curves without obvious IR drops at all current densities, suggesting low intrinsic resistance and rapid charge/discharge kinetics.

Figure 10a summarizes the areal capacitances of the prepared electrodes at different current densities. The capacitances of all freestanding electrodes decreased as the current density increased because of the limited electrolyte ion accessibility to the internal redox sites at higher current densities resulting in insufficient use of the PPy. The capacitance decay at high current densities was less significant for the *f*-CNT freestanding electrode than it was for the PPyNP/*f*-CNT and PPyC/*f*-CNT electrodes because of its excellent conductivity and mesoporous structure. Nevertheless, the PPyNP/*f*-CNT freestanding electrode displayed a high capacitance retention of 2752 mF cm^{-2} at a 10 mA cm^{-2} current density.

EIS tests of the freestanding electrodes were performed to obtain further information regarding the electrochemical characteristics (Figure 10b). The intercept of the semicircle in the high-frequency region is known as the equivalent series resistance (ESR), which consists of combined intrinsic resistances of the electrode materials and the electrolyte.[53,54] The low ESR in the high-frequency region and the lack of a semicircle for the pure *f*-CNT-based electrode indicate that its rapid and reversible charge storage kinetics was due to high conductivity.[55] The Nyquist plots of the composite electrodes featured semicircles at high frequencies, indicating the existence of charge transfer resistance across the interface of the electrode and electrolyte. The vertical lines with slopes at low frequencies correspond to diffusion of electrolyte in the porous active materials.[51,53,56] The PPyNP/*f*-CNT composite with a porous morphology resulted in the low electrolyte resistance in the pores of the active material.[54] As a result, the ESR of the PPyNP/*f*-CNT-based electrode (ca. 2.99 Ω) was lower than the ESR of the PPyC/*f*-CNT electrode (ca. 3.86 Ω). Figure S3a displays the cycling stability of the PPyNP/*f*-
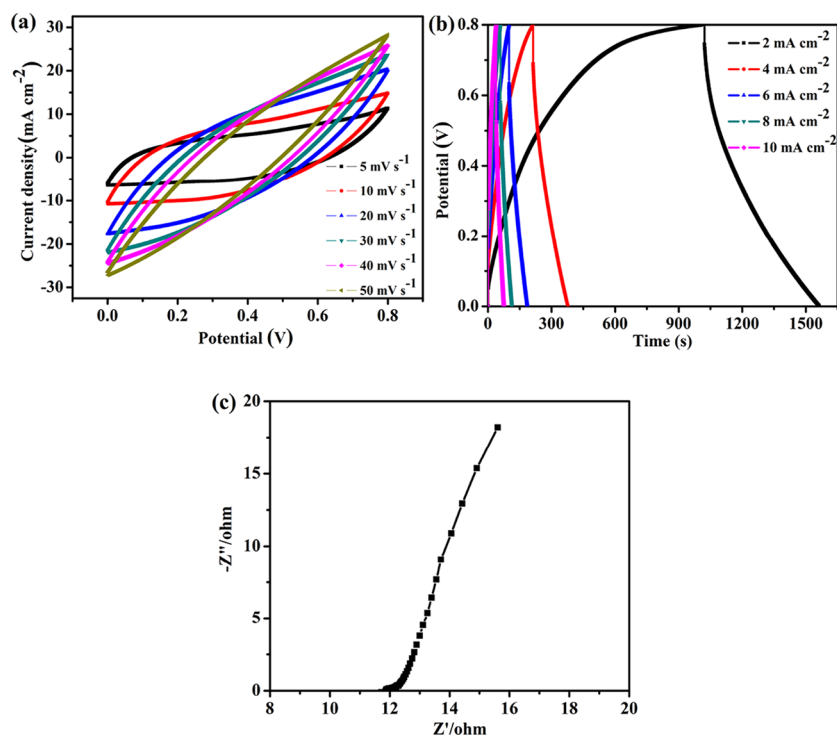
Figure 11. Electrochemical behaviors of the symmetric supercapacitor. (a) CV and (b) GCD plots at various scan rates and current densities, respectively. (c) EIS spectrum.
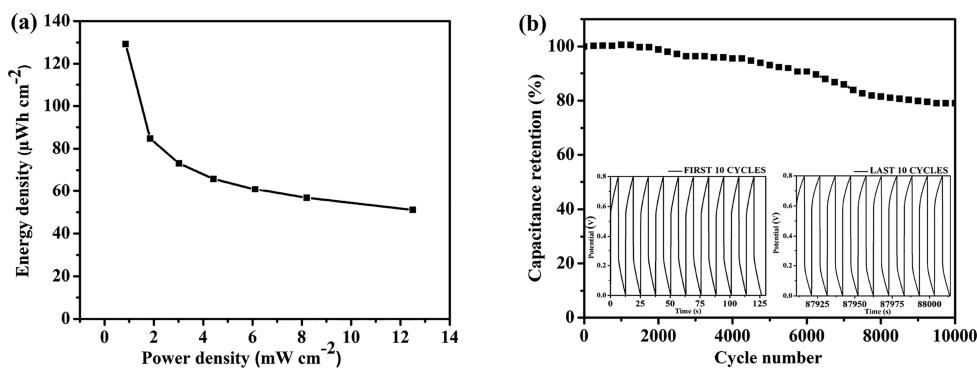
Figure 12. (a) Ragone plot and (b) cycle life test (10,000 cycles at 20 mA cm^{-2}) of the symmetric supercapacitor cell.

CNT freestanding electrode recorded at a high current density of 60 mA cm^{-2} for 10,000 charge/discharge cycles. The freestanding electrode exhibited good cycling stability with the retention of 71.6% of the initial capacitance after 10,000 charge/discharge cycles. The SEM images of the PPyNP/*f*-CNT freestanding electrode exhibited similar morphologies before (Figure 3c) and after the cycle test (Figure S3b). This suggests that the volume changes of PPyNP that occurred during ion doping and dedoping processes did not cause the separation of PPyNP and *f*-CNT. The electrochemical tests revealed that the PPyNP/*f*-CNT-based composite has a better performance than the PPyC/*f*-CNT electrode. We attribute the excellent capacitance performance of the PPyNP/*f*-CNT-based electrode to (i) the high active-material mass loadings; (ii) the high active surface area of the freestanding electrode, providing more redox sites for charge storage; (iii) the higher material use, resulting from the synergistic effect between the highly conductive *f*-CNTs and PPy; (iv) the increase in interfacial contact between the small PPy nanoparticles and the electrolyte; (v) the interconnected porous structure, which

provided electrolyte reservoirs that ensured efficient infiltration of the electrolyte into the entire porous matrix of the electrode material; (vi) the high electrical conductivity, which facilitated rapid charge transport; and (vii) the good wettability of the electrode.

To further study the electrochemical properties for practical applications, a symmetric supercapacitor device was fabricated using two identical PPyNP/*f*-CNT freestanding electrodes and a PVA/H$_2$SO$_4$ gel electrolyte. The quasi-rectangular-shaped CV curves indicate a combination of EDL capacitance and pseudocapacitance toward charge storage (Figure 11a). The charge/discharge tests were performed to further evaluate the capacitance properties of the supercapacitor device (Figure 11b). The nonlinear shapes of the GCD curves, indicative of Faradaic redox reactions, are in well agreement with the CV results. The slow diffusion of ions in the gel electrolyte and the poor interfacial contact between the gel electrolyte and the electrode material resulted in a large IR drop in the discharge curve and reduced areal capacitance at higher specific currents.[57] The areal, gravimetric, and volumetric capacitances

of the assembled supercapacitor were estimated using eqs 3, 4, and 7. The supercapacitor exhibited superior areal (1454.06 mF cm^{-2}), gravimetric (103.86 F g^{-1}), and volumetric capacitances (17.52 F cm^{-3}) at a current density of 2 mA cm^{-2}. Figure 11c presents the impedance plot of the supercapacitor cell. The Nyquist plot featured a semicircle and a vertical line at high and low frequencies, respectively, suggesting good capacitance performance. The ESR of the supercapacitor cell was approximately 11.88 Ω.

The energy and power densities were estimated based on the GCD data; Figure 12a shows the corresponding Ragone plot. The prepared supercapacitor device exhibited maximum areal (gravimetric, volumetric) energy densities of 129.24 μW h cm^{-2} (9.23 W h kg^{-1}, 1.56 mW h cm^{-3}) with power densities of 0.858 mW cm^{-2} (61.31 W kg^{-1}, 10.34 mW cm^{-3}). The device maintained areal (gravimetric, volumetric) energy densities of 51.06 μW h cm^{-2} (3.65 W h kg^{-1}, 615.18 μW h cm^{-3}) at maximum power densities of 12.5 mW cm^{-2} (892.86 W kg^{-1}, 150.6 mW cm^{-3}). The areal/gravimetric/volumetric capacitances and energy/power densities of the PPyNP/f-CNT electrode-based supercapacitor device were considerably larger than those of other literature-reported PPy-based supercapacitors, including a CNFs/rGO/PPy aerogel (720 mF cm^{-2}, 60.4 μW h cm^{-2} at 0.1 mW cm^{-2}),[58] RGO/PPy/cellulose hybrid papers (510 mF cm^{-2}, 1.18 mW h cm^{-3}), a PPy-coated air-laid paper (702 mF cm^{-2}, 62.4 μW h cm^{-2} at 0.42 mW cm^{-2}),[59] a KF@PPy/f-CNT-based electrode (258 mF cm^{-2}, 22.3 μW h cm^{-2} at 0.21 mW cm^{-2}),[8] an lCNT-GO/PPy composite electrode (72.3 mF cm^{-2}, 6.3 μW h cm^{-2}, 3.7 mW cm^{-2}),[60] and an RGO/PPy CCFs electrode (363 mF cm^{-2}, 0.28 mW h cm^{-3} at 20.9 mW cm^{-3}).[61] Despite having many attractive features, supercapacitor electrodes based on PPy have a major shortcoming of poor cycling charge−discharge stability due to repeated swelling and contracting of the polymer chains while undergoing charging and discharging, respectively. Thus, the capacitance degradation that occurs during prolonged cycling due to the volume changes caused by the insertion and de-insertion of counterions limits their practical applications.[10,62,63] Figure 12b displays the cycling stability of the supercapacitor tested at a high galvanostatic charge/discharge current density of 20 mA cm^{-2}. Capacitance retention with 79.03% of the initial capacitance after 10,000 cycles confirms the superior cycling charge/discharge stability of the supercapacitor cell. We attribute this remarkable cycle life to the morphological flexibility of the PPy nanoparticle, thereby accommodating the swell−shrink behavior of the polymeric backbone during long-term cycling.[64]

3. CONCLUSIONS

We have prepared PPy nanoparticles by using curcumin, a renewable biomaterial, as the structure-directing agent. A highly porous film was obtained having a high surface area and conductivity after blending the as-prepared PPy nanoparticles with f-CNTs. This film was then used as a freestanding electrode for supercapacitors. The PPyNP/f-CNT-based electrode exhibited superior areal capacitance (4585 mF cm^{-2}) and volumetric capacitance (176.35 F cm^{-3}) at 2 mA cm^{-2}. The remarkable electrochemical performance of the as-prepared composite electrode was ascribed to the high active-material mass loadings, the large effective surface area, the synergy between the highly conductive f-CNTs and the pseudocapacitive PPy, the increased interfacial contact between the small PPy nanoparticles and the electrolyte, and

the interconnected porous morphology and excellent conductivity of the electrode. A symmetric all-solid-state cell based on the freestanding PPyNP/f-CNT-based electrodes exhibited maximum areal energy and power densities of 64.62 μW h cm^{-2} and 6.25 mW cm^{-2}, respectively. Besides, the cell also exhibited superior cycle stability with a retention of 79.03% capacitance after 10,000 charge/discharge cycles. These results suggest the potential application of the PPyNP/f-CNT composite in all-solid-state supercapacitors.

4. EXPERIMENTAL SECTION

4.1. Materials. The CNTs were purchased from C-nano Technology (China). Curcumin [1,7-bis(4-hydroxy-3-methoxyphenyl)-1,6-heptadiene-3,5-dione], poly(vinyl alcohol) (PVA), sulfuric acid (H$_2$SO$_4$), ferric chloride hexahydrate (FeCl$_3$·6H$_2$O), nitric acid (HNO$_3$), and ethanol (C$_2$H$_5$OH) were procured from Showa Chemical Industry (Japan). Pyrrole was procured from Alfa Aesar (UK), which was distilled under reduced pressure prior to use.

4.2. PPy Nanoparticles (PPyNP). Curcumin and pyrrole were dissolved in anhydrous ethanol (50 mL). The precipitation of curcumin was induced by the addition of DI water (200 mL). The dropwise addition of an aqueous solution of ferric chloride initiated the polymerization reaction; the molar ratio of pyrrole to ferric chloride was kept as 1:1.5. After performing the polymerization reaction for 4 h, the sediments were separated and thoroughly washed with DI water. The curcumin template was removed completely by soaking in anhydrous ethanol. The obtained PPy was rewashed with DI water and vacuum-dried in an oven. The PPy nanoparticle sample prepared using the curcumin template is denoted herein as "PPyNP"; the control sample was prepared under the same conditions but without the curcumin template is denoted as "PPyC".

4.3. PPy Nanoparticle/f-CNT Composite Film. To prepare the functionalized CNTs, raw CNTs were refluxed at 90 °C using 3 M HNO$_3$ for 14 h. The treated CNTs were then sonicated for 1 h, filtered, washed, and dried to obtain functionalized CNTs (f-CNTs).[65] The as-synthesized PPyNP and f-CNTs were dispersed separately in ethanol through ultrasonication. The dispersions were thoroughly mixed by magnetic stirring and ultrasonication before filtered off to form the PPyNP/f-CNT composite film. The PPyC/f-CNT composite film was prepared from PPyC using the same method. The mass ratio of PPyNP and f-CNT was fixed at 8:2. The composite films prepared using PPyNP and PPyC are denoted herein as "PPyNP/f-CNT" and "PPyC/f-CNT", respectively. The thickness of the PPyNP/f-CNT nanocomposite film was approximately 260 μm.

4.4. Characterization. A PerkinElmer Spectrum RX1 FTIR spectrophotometer and pressed KBr pellets of the PPyNP/f-CNT composites were used to measure the Fourier transform infrared (FTIR) spectra. Morphologies of the composite films were analyzed using scanning electron microscopy (SEM, JSM 7401F). A drop of the sample dispersed in ethanol was placed on a Cu grid to collect the TEM images of dried samples using a transmission electron microscope (TEM, JEOL JEM-1400). In addition, X-ray diffraction (XRD) images were studied using a Rigaku RINT 2000 diffractometer (Tokyo, Japan). Contact angle measurements were taken using a contact angle meter (JC2000D1, Shanghai Zhongchen Digital Technic Apparatus, China). A Micromeritics surface area and porosity analyzer (ASAP 2010,

USA) was used to record the nitrogen sorption isotherms of the composites. The Brunauer−Emmett−Teller (BET) and Barret−Joyner−Halenda (BJH) calculations were used to confirm the specific surface areas and pore size distributions, respectively, of the composite films.

4.5. Electrochemical Characterization of the Free-standing Composite Electrodes. A CHI6273D electrochemical workstation (CH Instruments, USA) was used to perform the electrochemical tests in a three-electrode system. A saturated calomel electrode (SCE), a piece of the composite film, platinum foil, and aqueous 1 M H_2SO_4 were employed as the reference electrode, working electrode, counter electrode, and electrolyte, respectively. CV and GCD experiments were performed at different scan rates and applied current densities, respectively, in the voltage range from −0.2 to +0.6 V. EIS tests were performed over the frequency range from 0.01 Hz to 100 kHz with an amplitude of 5 mV.

The areal capacitances (C_A, F cm^{-2}) were estimated using eq 1 from the GCD curve[8]

$$C_A = \frac{I\Delta t}{A \times \Delta V} \tag{1}$$

where ΔV represents the potential window (V) excluding the IR drop, I is the discharge current (A), Δt is the discharge time (s), and A is the area of the freestanding electrode (cm^2). The gravimetric capacitance (C_m, F g^{-1}) is calculated by replacing A by m, the mass of the freestanding electrode (g) in eq 1 .

The volumetric capacitance (C_V, F cm^{-3}) was calculated using eq 2[8]

$$C_V = \frac{C_A}{d} \tag{2}$$

where d is the thickness of the freestanding electrode (cm).

4.6. Electrochemical Performance Evaluation of the Symmetric Supercapacitor Device. For the preparation of the H_2SO_4/PVA-based gel electrolyte, PVA powder (1 g) and H_2SO_4 (1 g) were dissolved in DI water (10 mL) at 85 °C by magnetic stirring. The symmetric supercapacitor cell was assembled using a filter paper and soaked in the H_2SO_4/PVA gel electrolyte and two pieces of PPyNP/f-CNT freestanding electrodes. The thickness of the assembled device was nearly 0.083 cm. The electrochemical behavior of the symmetric supercapacitor cell was characterized using a CHI6273D (CH Instruments, USA) electrochemical work station. The areal ($C_{a−cell}$, F cm^{-2}) and gravimetric capacitance ($C_{m−cell}$, F g^{-1}) of the cell was estimated according to eqs 3 and 4[8]

$$C_{a-cell} = \frac{I\Delta t}{A \times \Delta V} \tag{3}$$

$$C_{m-cell} = \frac{I\Delta t}{m \times \Delta V} \tag{4}$$

The energy (E, μW h cm^{-2}) and power densities (P, μW cm^{-2}) of the supercapacitor cell were estimated using eqs 6 and 7[8]

$$E = \frac{1}{2}\frac{C_{cell}V^2}{3.6} \tag{5}$$

$$P = \frac{E \times 3600}{\Delta t} \tag{6}$$

The volumetric capacitance ($C_{V−cell}$, F cm^{-3}) was estimated using eq 5

$$C_{V-cell} = \frac{C_{cell}}{d} \tag{7}$$

where ΔV represents the potential window (V) excluding the IR drop, I is the discharge current (A), Δt is the discharge time (s), d is the thickness of the supercapacitor cell (cm), m is the mass of the active material loaded on a single electrode, and A is the area of a single electrode (cm^2).

■ ASSOCIATED CONTENT

ⓈI Supporting Information

The Supporting Information is available free of charge at https://pubs.acs.org/doi/10.1021/acsomega.9b04029.

XRD pattern and FTIR spectrum of curcumin (Figure S1); the nitrogen sorption isotherm and pore size distribution curve (Figure S2); cyclic performance and the SEM image after cycling test (Figure S3); capacitive performances of PPy-based composite electrodes reported previously in the literature and in this present study (Table S1) (PDF)

■ AUTHOR INFORMATION

Corresponding Author

Rong-Ho Lee − *Department of Chemical Engineering, National Chung Hsing University, Taichung 402, Taiwan;* ⓘ orcid.org/0000-0002-1373-9360; Email: rhl@nchu.edu.tw

Authors

Jincy Parayangattil Jyothibasu − *Department of Chemical Engineering and Department of Environmental Engineering, National Chung Hsing University, Taichung 402, Taiwan;* ⓘ orcid.org/0000-0003-4415-328X

Ming-Zhu Chen − *Department of Chemical Engineering, National Chung Hsing University, Taichung 402, Taiwan*

Complete contact information is available at:
https://pubs.acs.org/10.1021/acsomega.9b04029

Notes

The authors declare no competing financial interest.

■ ACKNOWLEDGMENTS

■ REFERENCES

(1) Gür, T. M. Review of electrical energy storage technologies, materials and systems: challenges and prospects for large-scale grid storage. *Energy Environ. Sci.* **2018**, *11*, 2696−2767.

(2) Zhang, Y.-Z.; Wang, Y.; Cheng, T.; Yao, L.-Q.; Li, X.; Lai, W.-Y.; Huang, W. Printed supercapacitors: materials, printing and applications. *Chem. Soc. Rev.* **2019**, *48*, 3229−3264.

(3) Wu, Z.; Li, L.; Yan, J.-M.; Zhang, X.-B. Materials Design and System Construction for Conventional and New-Concept Supercapacitors. *Adv. Sci.* **2017**, *4*, 1600382.

(4) Cao, A.; Chen, Z.; Wang, Y.; Zhang, J.; Wang, Y.; Li, T.; Han, Y. Redox-active doped polypyrrole microspheres induced by phosphomolybdic acid as supercapacitor electrode materials. *Synth. Met.* **2019**, *252*, 135−141.

(5) Ahn, K.-J.; Lee, Y.; Choi, H.; Kim, M.-S.; Im, K.; Noh, S.; Yoon, H. Surfactant-Templated Synthesis of Polypyrrole Nanocages as Redox Mediators for Efficient Energy Storage. *Sci. Rep.* **2015**, *5*, 14097.

(6) Singh, A. K.; Mandal, K. Engineering of high performance supercapacitor electrode based on Fe-Ni/Fe2O3-NiO core/shell hybrid nanostructures. *J. Appl. Phys.* **2015**, *117*, 105101.

(7) Shown, I.; Ganguly, A.; Chen, L.-C.; Chen, K.-H. Conducting polymer-based flexible supercapacitor. *Energy Sci. Eng.* **2015**, *3*, 2−26.

(8) Jyothibasu, J.; Lee, R.-H. Facile, Scalable, Eco-Friendly Fabrication of High-Performance Flexible All-Solid-State Supercapacitors. *Polymer* **2018**, *10*, 1247.

(9) Xu, J.; Zhu, L.; Bai, Z.; Liang, G.; Liu, L.; Fang, D.; Xu, W. Conductive polypyrrole−bacterial cellulose nanocomposite membranes as flexible supercapacitor electrode. *Org. Electron.* **2013**, *14*, 3331−3338.

(10) Zhao, J.; Wu, J.; Li, B.; Du, W.; Huang, Q.; Zheng, M.; Xue, H.; Pang, H. Facile synthesis of polypyrrole nanowires for high-performance supercapacitor electrode materials. *Prog. Nat. Sci.: Mater. Int.* **2016**, *26*, 237−242.

(11) An, H.; Wang, Y.; Wang, X.; Zheng, L.; Wang, X.; Yi, L.; Bai, L.; Zhang, X. Polypyrrole/carbon aerogel composite materials for supercapacitor. *J. Power Sources* **2010**, *195*, 6964−6969.

(12) Li, Z.; Cai, J.; Cizek, P.; Niu, H.; Du, Y.; Lin, T. A self-supported, flexible, binder-free pseudo-supercapacitor electrode material with high capacitance and cycling stability from hollow, capsular polypyrrole fibers. *J. Mater. Chem. A* **2015**, *3*, 16162−16167.

(13) Song, Y.; Liu, T.-Y.; Xu, X.-X.; Feng, D.-Y.; Li, Y.; Liu, X.-X. Pushing the Cycling Stability Limit of Polypyrrole for Supercapacitors. *Adv. Funct. Mater.* **2015**, *25*, 4626−4632.

(14) Choudhary, N.; Li, C.; Moore, J.; Nagaiah, N.; Zhai, L.; Jung, Y.; Thomas, J. Asymmetric Supercapacitor Electrodes and Devices. *Adv. Mater.* **2017**, *29*, 1605336.

(15) Liu, P.; Wang, X.; Wang, Y. Design of Carbon Black/Polypyrrole Composite Hollow Nanospheres and Performance Evaluation as Electrode Materials for Supercapacitors. *ACS Sustainable Chem. Eng.* **2014**, *2*, 1795−1801.

(16) Lee, J.; Jeong, H.; Lassarote Lavall, R.; Busnaina, A.; Kim, Y.; Jung, Y. J.; Lee, H. Polypyrrole Films with Micro/Nanosphere Shapes for Electrodes of High-Performance Supercapacitors. *ACS Appl. Mater. Interfaces* **2017**, *9*, 33203−33211.

(17) Wang, J.; Cao, Y.; Lu, Y. Size-controllable polypyrrole nanospheres synthesized in the presence of phosphorylated chitosan and their size effect in different applications. *J. Nanopart. Res.* **2015**, *17*, 236.

(18) Yang, X.; Lin, Z.; Zheng, J.; Huang, Y.; Chen, B.; Mai, Y.; Feng, X. Facile template-free synthesis of vertically aligned polypyrrole nanosheets on nickel foams for flexible all-solid-state asymmetric supercapacitors. *Nanoscale* **2016**, *8*, 8650−8657.

(19) Huang, S.; Han, Y.; Lyu, S.; Lin, W.; Chen, P.; Fang, S. A facile one-step approach for the fabrication of polypyrrole nanowire/carbon fiber hybrid electrodes for flexible high performance solid-state supercapacitors. *Nanotechnology* **2017**, *28*, 435204.

(20) Xu, J.; Wang, D.; Fan, L.; Yuan, Y.; Wei, W.; Liu, R.; Gu, S.; Xu, W. Fabric electrodes coated with polypyrrole nanorods for flexible supercapacitor application prepared via a reactive self-degraded template. *Org. Electron.* **2015**, *26*, 292−299.

(21) Lee, S.; Cho, M.-S.; Nam, J.-D.; Lee, Y. Fabrication of Polypyrrole Nanorod Arrays for Supercapacitor: Effect of Length of Nanorods on Capacitance. *J. Nanosci. Nanotechnol.* **2008**, *8*, 5036−5041.

(22) Lei, W.; He, P.; Wang, Y.; Zhang, S.; Dong, F.; Liu, H. Soft template interfacial growth of novel ultralong polypyrrole nanowires for electrochemical energy storage. *Electrochim. Acta* **2014**, *132*, 112−117.

(23) Santino, L. M.; Acharya, S.; D'Arcy, J. M. Low-temperature vapour phase polymerized polypyrrole nanobrushes for supercapacitors. *J. Mater. Chem. A* **2017**, *5*, 11772−11780.

(24) Li, M.; Yang, L.; Zhang, Y. Hierarchical structure of hollow thorn-like polypyrrole microtubes with enhanced electrochemical performance. *RSC Adv.* **2015**, *5*, 1191−1197.

(25) Feng, J.; Lv, W.; Liu, J.; Li, J.; Yang, H.; Xu, H.; Yan, W. Enhanced capacitance of rectangular-sectioned polypyrrole micro-

tubes as the electrode material for supercapacitors. *RSC Adv.* **2014**, *4*, 40686−40692.

(26) Santino, L. M.; Hwang, E.; Diao, Y.; Lu, Y.; Wang, H.; Jiang, Q.; Singamaneni, S.; D'Arcy, J. M. Condensing Vapor Phase Polymerization (CVPP) of Electrochemically Capacitive and Stable Polypyrrole Microtubes. *ACS Appl. Mater. Interfaces* **2017**, *9*, 41496−41504.

(27) Qu, L.; Shi, G.; Chen, F.; Zhang, J. Electrochemical Growth of Polypyrrole Microcontainers. *Macromolecules* **2003**, *36*, 1063−1067.

(28) Shi, Y.; Pan, L.; Liu, B.; Wang, Y.; Cui, Y.; Bao, Z.; Yu, G. Nanostructured conductive polypyrrole hydrogels as high-performance, flexible supercapacitor electrodes. *J. Mater. Chem. A* **2014**, *2*, 6086−6091.

(29) Tong, L.; Gao, M.; Jiang, C.; Cai, K. Ultra-high performance and flexible polypyrrole coated CNT paper electrodes for all-solid-state supercapacitors. *J. Mater. Chem. A* **2019**, *7*, 10751−10760.

(30) Su, Y.; Zhitomirsky, I. Asymmetric electrochemical supercapacitor, based on polypyrrole coated carbon nanotube electrodes. *Appl. Energy* **2015**, *153*, 48−55.

(31) Lee, K. Y. T.; Shi, H. H.; Lian, K.; Naguib, H. E. Flexible multiwalled carbon nanotubes/conductive polymer composite electrode for supercapacitor applications. *Smart Mater. Struct.* **2015**, *24*, 115008.

(32) Zhang, B.; Xu, Y.; Zheng, Y.; Dai, L.; Zhang, M.; Yang, J.; Chen, Y.; Chen, X.; Zhou, J. A Facile Synthesis of Polypyrrole/Carbon Nanotube Composites with Ultrathin, Uniform and Thickness-Tunable Polypyrrole Shells. *Nanoscale Res. Lett.* **2011**, *6*, 431.

(33) Zhou, Y.; Hu, X.; Shang, Y.; Hua, C.; Song, P.; Li, X.; Zhang, Y.; Cao, A. Highly flexible all-solid-state supercapacitors based on carbon nanotube/polypyrrole composite films and fibers. *RSC Adv.* **2016**, *6*, 62062−62070.

(34) Yesi, Y.; Shown, I.; Ganguly, A.; Ngo, T. T.; Chen, L.-C.; Chen, K.-H. Directly-Grown Hierarchical Carbon Nanotube@Polypyrrole Core−Shell Hybrid for High-Performance Flexible Supercapacitors. *ChemSusChem* **2016**, *9*, 370−378.

(35) Asen, P.; Shahrokhian, S. A High Performance Supercapacitor Based on Graphene/Polypyrrole/Cu2O−Cu(OH)2 Ternary Nanocomposite Coated on Nickel Foam. *J. Phys. Chem. C* **2017**, *121*, 6508−6519.

(36) Díez, N.; Botas, C.; Mysyk, R.; Goikolea, E.; Rojo, T.; Carriazo, D. Highly packed graphene−CNT films as electrodes for aqueous supercapacitors with high volumetric performance. *J. Mater. Chem. A* **2018**, *6*, 3667−3673.

(37) Bakandritsos, A.; Jakubec, P.; Pykal, M.; Otyepka, M. Covalently functionalized graphene as a supercapacitor electrode material. *FlatChem* **2019**, *13*, 25−33.

(38) Zhu, Y.; Shi, K.; Zhitomirsky, I. Anionic dopant−dispersants for synthesis of polypyrrole coated carbon nanotubes and fabrication of supercapacitor electrodes with high active mass loading. *J. Mater. Chem. A* **2014**, *2*, 14666−14673.

(39) Hewlings, S.; Kalman, D. Curcumin: A Review of Its' Effects on Human Health. *Foods* **2017**, *6*, 92.

(40) Hazra, M. K.; Roy, S.; Bagchi, B. Hydrophobic hydration driven self-assembly of curcumin in water: Similarities to nucleation and growth under large metastability, and an analysis of water dynamics at heterogeneous surfaces. *J. Chem. Phys.* **2014**, *141*, 18C501.

(41) Gupta, S. C.; Prasad, S.; Kim, J. H.; Patchva, S.; Webb, L. J.; Priyadarsini, I. K.; Aggarwal, B. B. Multitargeting by curcumin as revealed by molecular interaction studies. *Nat. Prod. Rep.* **2011**, *28*, 1937−1955.

(42) Alem, M.; Tarlani, A.; Aghabozorg, H. R. Synthesis of nanostructured alumina with ultrahigh pore volume for pH-dependent release of curcumin. *RSC Adv.* **2017**, *7*, 38935−38944.

(43) Singh, P. K.; Wani, K.; Kaul-Ghanekar, R.; Prabhune, A.; Ogale, S. From micron to nano-curcumin by sophorolipid co-processing: highly enhanced bioavailability, fluorescence, and anti-cancer efficacy. *RSC Adv.* **2014**, *4*, 60334−60341.

(44) Cao, J.; Wang, Y.; Chen, J.; Li, X.; Walsh, F. C.; Ouyang, J.-H.; Jia, D.; Zhou, Y. Three-dimensional graphene oxide/polypyrrole

composite electrodes fabricated by one-step electrodeposition for high performance supercapacitors. *J. Mater. Chem. A* **2015**, *3*, 14445−14457.

(45) Zhou, H.; Han, G.; Xiao, Y.; Chang, Y.; Zhai, H.-J. Facile preparation of polypyrrole/graphene oxide nanocomposites with large areal capacitance using electrochemical codeposition for supercapacitors. *J. Power Sources* **2014**, *263*, 259−267.

(46) Dubal, D. P.; Lee, S. H.; Kim, J. G.; Kim, W. B.; Lokhande, C. D. Porous polypyrrole clusters prepared by electropolymerization for a high performance supercapacitor. *J. Mater. Chem.* **2012**, *22*, 3044−3052.

(47) Wan, C.; Jiao, Y.; Li, J. Flexible, highly conductive, and free-standing reduced graphene oxide/polypyrrole/cellulose hybrid papers for supercapacitor electrodes. *J. Mater. Chem. A* **2017**, *5*, 3819−3831.

(48) Fan, L.-Q.; Liu, G.-J.; Wu, J.-H.; Liu, L.; Lin, J.-M.; Wei, Y.-L. Asymmetric supercapacitor based on graphene oxide/polypyrrole composite and activated carbon electrodes. *Electrochim. Acta* **2014**, *137*, 26−33.

(49) Zhang, Y.-J.; Xue, J.-Q.; Li, F.; Dai, J.-Z.; Zhang, X.-Z.-Y. Preparation of polypyrrole/chitosan/carbon nanotube composite nano-electrode and application to capacitive deionization process for removing Cu^{2+}. *Chem. Eng. Process.* **2019**, *139*, 121−129.

(50) Anwar, M.; Ahmad, I.; Warsi, M. H.; Mohapatra, S.; Ahmad, N.; Akhter, S.; Ali, A.; Ahmad, F. J. Experimental investigation and oral bioavailability enhancement of nano-sized curcumin by using supercritical anti-solvent process. *Eur. J. Pharm. Biopharm.* **2015**, *96*, 162−172.

(51) Zhou, Y.; Candelaria, S. L.; Liu, Q.; Huang, Y.; Uchaker, E.; CaO, G. Sulfur-rich carbon cryogels for supercapacitors with improved conductivity and wettability. *J. Mater. Chem. A* **2014**, *2*, 8472−8482.

(52) Kakade, B. A.; Pillai, V. K. Tuning the Wetting Properties of Multiwalled Carbon Nanotubes by Surface Functionalization. *J. Phys. Chem. C* **2008**, *112*, 3183−3186.

(53) Liu, Q.; Chen, Z.; Jing, S.; Zhuo, H.; Hu, Y.; Liu, J.; Zhong, L.; Peng, X.; Liu, C. A foldable composite electrode with excellent electrochemical performance using microfibrillated cellulose fibers as a framework. *J. Mater. Chem. A* **2018**, *6*, 20338−20346.

(54) Wang, L.; Ji, H.; Wang, S.; Kong, L.; Jiang, X.; Yang, G. Preparation of Fe_3O_4 with high specific surface area and improved capacitance as a supercapacitor. *Nanoscale* **2013**, *5*, 3793−3799.

(55) Zhao, J.; Li, Y.; Wang, G.; Wei, T.; Liu, Z.; Cheng, K.; Ye, K.; Zhu, K.; Cao, D.; Fan, Z. Enabling high-volumetric-energy-density supercapacitors: designing open, low-tortuosity heteroatom-doped porous carbon-tube bundle electrodes. *J. Mater. Chem. A* **2017**, *5*, 23085−23093.

(56) Kim, M. S.; Moon, J. H.; Yoo, P. J.; Park, J. H. Hollow Polypyrrole Films: Applications for Energy Storage Devices. *J. Electrochem. Soc.* **2012**, *159*, A1052−A1056.

(57) Ma, L.; Fan, H.; Wei, X.; Chen, S.; Hu, Q.; Liu, Y.; Zhi, C.; Lu, W.; Zapien, J. A.; Huang, H. Towards high areal capacitance, rate capability, and tailorable supercapacitors: Co3O4@polypyrrole core−shell nanorod bundle array electrodes. *J. Mater. Chem. A* **2018**, *6*, 19058−19065.

(58) Zhang, Y.; Shang, Z.; Shen, M.; Chowdhury, S. P.; Ignaszak, A.; Sun, S.; Ni, Y. Cellulose Nanofibers/Reduced Graphene Oxide/Polypyrrole Aerogel Electrodes for High-Capacitance Flexible All-Solid-State Supercapacitors. *ACS Sustainable Chem. Eng.* **2019**, *7*, 11175−11185.

(59) Chen, Y.; Cai, K.; Liu, C.; Song, H.; Yang, X. High-Performance and Breathable Polypyrrole Coated Air-Laid Paper for Flexible All-Solid-State Supercapacitors. *Adv. Energy Mater.* **2017**, *7*, 1701247.

(60) Zhou, H.; Zhai, H.-J. A highly flexible solid-state supercapacitor based on the carbon nanotube doped graphene oxide/polypyrrole composites with superior electrochemical performances. *Org. Electron.* **2016**, *37*, 197−206.

(61) Lyu, S.; Chang, H.; Fu, F.; Hu, L.; Huang, J.; Wang, S. Cellulose-coupled graphene/polypyrrole composite electrodes containing conducting networks built by carbon fibers as wearable supercapacitors with excellent foldability and tailorability. *J. Power Sources* **2016**, *327*, 438−446.

(62) Snook, G. A.; Kao, P.; Best, A. S. Conducting-polymer-based supercapacitor devices and electrodes. *J. Power Sources* **2011**, *196*, 1−12.

(63) Zhao, C.; Shu, K.; Wang, C.; Gambhir, S.; Wallace, G. G. Reduced graphene oxide and polypyrrole/reduced graphene oxide composite coated stretchable fabric electrodes for supercapacitor application. *Electrochim. Acta* **2015**, *172*, 12−19.

(64) Jyothibasu, J. P.; Lee, R.-H. Green synthesis of polypyrrole tubes using curcumin template for excellent electrochemical performance in supercapacitors. *J. Mater. Chem. A* **2020**, *8*, 3186−3202.

(65) Jyothibasu, J. P.; Kuo, D.-W.; Lee, R.-H. Flexible and freestanding electrodes based on polypyrrole/carbon nanotube/cellulose composites for supercapacitor application. *Cellulose* **2019**, *26*, 4495−4513.